Surface & Coatings Technology 429 (2022) 127921

Contents lists available at ScienceDirect

Surface & Coatings Technology

journal homepage: www.elsevier.com/locate/surfcoat

Construction of a compact nanocrystal structure for $(CrNbTiAlV)N_x$ high-entropy nitride films to improve the tribo-corrosion performance

Cunxiu Zhang [a,b], Xiaolong Lu [b,c], Haibin Zhou [b,c], Yanfang Wang [a,*], Xudong Sui [b,c,**], ZhiQiang Shi [a], Junying Hao [b]

[a] School of Materials Science and Engineering, China University of Petroleum (East China), Qingdao 266580, China
[b] State Key Laboratory of Solid Lubrication, Lanzhou Institute of Chemical Physics, Chinese Academy of Science, Lanzhou 730000, China
[c] Qingdao Center of Resource Chemistry and New Materials, Qingdao 266000, China

ARTICLE INFO

Keywords:
High-entropy nitride films
Substrate bias
Microstructure
Tribo-corrosion performance
Magnetron sputtering

ABSTRACT

$(CrNbTiAlV)N_x$ high-entropy nitride films were prepared using magnetron sputtering method. The effect of substrate bias on the microstructure, mechanical, electrochemical, and tribo-corrosion properties of the films was systematically studied. The results show that the microstructure of the film changes from a loose columnar structure to a compact nanocrystal structure with the increase of substrate bias, accompanied by the preferred orientation from (200) to (111). The hardness, modulus and residual stress are positively correlated with increased substrate bias, reaching the maximum values of 35.3 GPa, 353.7 GPa and −6.41 GPa at −156 V, respectively. Under static corrosion, the film deposited under −126 V has the most positive E_{corr} of −0.05 V and the lowest i_{corr} of 0.013 μA/cm^2. Under tribo-corrosion, the films deposited at −96 V and −126 V show the lowest coefficient of friction (~0.2) and wear rate (~4.4×10^{-7} mm^3·N^{-1}·m^{-1}), respectively. The evolution of microstructure and mechanical property are the main factors affecting the tribo-corrosion behavior of $(CrNbTiAlV)N_x$ films.

1. Introduction

Recently, tribo-corrosion has become the worldwide concern for marine industry. Moving parts need to withstand the dual effects of friction and wear and seawater corrosion when they are used in the marine environment, which is usually called tribo-corrosion [1]. Metal materials (titanium alloy, aluminum alloy, stainless steel, etc.) are often taken as a material of choice in the design of marine components due to their excellent corrosion response with the evolution of a continuously regenerated oxide passivation film on its surface [2–4]. However, due to their poor tribological properties, if they are directly used as moving parts, the coupling effect of friction and corrosion will accelerate the loss of materials, which may cause accidents and waste of resources [5]. Therefore, there is a great need for protective coating with anti-corrosion and anti-wear to prolong the service life of mechanical components in marine applications [6].

Over the past decade, high-entropy alloys (HEAs) have been demonstrated as promising materials for various applications due to their excellent properties in mechanics, physics and chemistry [7]. Based on high-entropy effect and rapid cooling effect, high-entropy films (HEFs) tend to form amorphous or single fcc and bcc structures [8,9]. The unique structure characteristic endows HEFs with excellent corrosion resistance as Marine anti-corrosion coating. However, high-entropy metallic films have low hardness and poor wear resistance. Therefore, many researchers consider doping some small radius non-metallic elements (such as C, N, B) into HEFs to improve the hardness [10]. Nowadays, high-entropy nitride films (HENFs), which inherit the characteristics of HEAs, have aroused the extensive research interest of scholars due to its high hardness, good thermal stability, excellent wear and corrosion resistance [11–15]. For example, Fieandt. et al. [13] successfully prepared (AlCrNbYZr)N film with the highest hardness of 30 GPa by adjusting the nitrogen content. Feng. et al. [14] found that the wear rate of multi-element (CrTaNbMoV)N film prepared at $R_N = 20\%$ is an order of magnitude lower than CrTaNbMoV metallic film ($R_N = 0\%$).

* Corresponding author.
** Correspondence to: X. Sui, State Key Laboratory of Solid Lubrication, Lanzhou Institute of Chemical Physics, Chinese Academy of Science, Lanzhou 730000, China.
E-mail addresses: wang@upc.edu.cn (Y. Wang), suixudong@licp.cas.cn (X. Sui).

https://doi.org/10.1016/j.surfcoat.2021.127921
Received 14 September 2021; Received in revised form 29 October 2021; Accepted 10 November 2021
Available online 16 November 2021

Chen. et al. [15] pointed that (VAlTiCrMo)N coating exhibited a higher E_{corr}, lower i_{corr} and wider passive range than its metallic coating due to the increase of non-metallicity. Furthermore, the densification of structure is one of the important factors affecting the corrosion resistance of films. The compact structure has low diffusion coefficient, resulting in high impedance to resist electrochemical corrosion [16]. In line with this, many methods have been proposed to improve the densification of the film structure, including element doping [17,18] and optimization of deposition parameters [19,20]. For instance, Shen et al. [19] realized the transformation of the structure of $(Al_{1.5}CrNb_{0.5}Si_{0.5}Ti)N$ coating from loose columnar to compact structure by adjusting the substrate bias, and obtained the highest hardness of 36 GPa at bias of −100 V. Hsueh et al. [20] researched that the synergistic effect of nitrogen flow and substrate bias on the structure and properties of $(AlCrSiTiZr)_{100-x}N_x$ film, and detected that substrate bias significantly improved its corrosion resistance. Based on the above analysis, high-entropy nitride films have promising properties to cope with harsh marine tribo-corrosion environment. However, there are few reports on the tribo-corrosion performances of HENFs.

In our group's previous studies [21], $(CrNbTiAlV)N_x$ high-entropy nitride coating showed a good tribological property in solid–liquid composite lubrication. However, the coating prepared has limited hardness and distinct columnar structure, which may not be advantageous in a tribo-corrosion environment. Therefore, this work aims to construct a compact structure for $(CrNbTiAlV)N_x$ high-entropy nitride films by tailoring substrate bias to improve the tribo-corrosion performance. The effects of substrate bias on microstructure, mechanical, electrochemical and tribo-corrosion performances of the films were systematically analyzed, as well as the influencing factors under static electrochemical and dynamic tribo-corrosion condition.

2. Experimental details

2.1. Film deposition and characterization

High-entropy nitride films of $(CrNbTiAlV)N_x$ were fabricated on AISI 440C steel (with a size of Φ25 × 4 mm) and silicon substrates (20 × 20 mm) via magnetron sputtering system (UDP-650, Teer PlasMag™) with a Cr-Nb-Ti-Al-V (99.99 wt% in purity) splicing target. The crystal structure and radius of selected elements were summarized in Table 1. All substrates were cleaned ultrasonically in petroleum ether and ethanol in turn before being placed in the center of vacuum chamber. The distance between the sample and the target is fixed at 12 cm. When the base pressure in chamber was reached 3×10^{-5} Torr, the pre-cleaning process with 18 standard cubic centimeter per minute (sccm) of Argon gas was operated to remove the oxides and pollutants on the substrate surface. After that, the Cr interlayer (~150 nm in thickness) was prepared for 8 min to improve the adhesion between the film and substrate. Then, with the nitrogen flow up to 38 sccm, $(CrNbTiAlV)N_x$ films were deposited at various substrate bias of −36 V, −66 V, −96 V, −126 V, and −156 V, denoted as S36, S66, S96, S126, and S156, respectively. The films prepared with similar thickness were obtained by adjusting the deposition time. The process parameters are listed in detail in Table 2.

The microstructure and element composition of all the samples were analyzed by the Field Emission Scanning Electron Microscopy (FESEM, JSM 7610F) equipped with Energy Dispersive Spectrometer (EDS, UltraDry). The root mean squared (RMS) roughness of the samples was evaluated by using the Atomic Force Microscopy (AFM, Nano Wizard 4). The phase structures were investigated by using the X-Ray Diffraction (XRD, Bruker D8 Advance) with the glancing angle of 1° and scanning range of 20°–80°. The hardness and modulus of the films were measured by Nano indenter (Agilent G200) with the continuous stiffness method. To eliminate the effect of the substrate on the film hardness, the indentation depth was set as 100 nm. Ten measurements were used to ensure the reliability of the data. The Poisson's ratio was 0.23. The adhesion of film and substrate was characterized by the Scratch Tester (MFT-4000, China) with the loading rate of 100 N/min and termination load of 100 N. The Film Stress Tester (FST 1000) was using to evaluate the residual stress σ of films and calculate from the Stoney equation [24]:

$$\sigma = \frac{E}{1-\nu}\frac{t^2}{6d}\left(\frac{1}{R_2}-\frac{1}{R_1}\right) \quad (1)$$

where E, t, ν, and R_1 are the young's modulus, thickness, Poisson ratio, and curvature radius of substrate, respectively. R_2 and d are the curvature radius and thickness of film in turn.

Table 1
The radius of each elements, crystal structure of metallic element and its nitride in $(CrNbTiAlV)N_x$ system at room temperature [22,23].

Element		Cr	Nb	Ti	Al	V	N
Radius (pm)		124.9	142.9	146.2	143.2	131.6	75
Crystal structure	Metal	bcc	bcc	hcp	fcc	bcc	–
	Nitride	fcc	fcc	fcc	hcp	fcc	–

Note: body-centered cubic structure (bcc), face-centered cubic structure (fcc), hexagonal close-packed structure (hcp).

Table 2
The details of the process parameters.

Process parameters	Pre-cleaning	Deposited films					
		Cr	HEFNs				
Current (A)	0.4	4.5	4.5				
N_2 flow (sccm)	0	0	38				
Ar flow (sccm)	18	18	18				
Working pressure (Torr)	2.5×10^{-3}	2.5×10^{-3}	4.1×10^{-3}				
Bias (V)	−450	−60	−36	−66	−96	−126	−156
Time (min)	30	8	270	270	300	300	330
Deposition temperature (°C)			No additional heating				

2.2. Electrochemical and tribo-corrosion tests

The electrochemical tests of all the samples were conducted in 3.5 wt % NaCl solution under room temperature using the electrochemical station (CS350, China). Potentiodynamic polarization (PD) tests were executed with a three-electrode cell where the samples (~1 m^2 of exposed area), platinum, and saturated calomel electrode (SCE) acted as the working electrode (WE), counter electrode (CE), and reference electrode (RE), respectively. The potential scanning range was set as −0.6 V to 1.2 V (vs. OCP) with a scanning speed of 1 mV/s. Before PD tests, the open circuit potential (OCP) was stabilized for ~1 h. The corrosion current density (i_{corr}) and corrosion potential (E_{corr}) were calculated by Tafel extrapolation. The tribo-corrosion (TC) tests of the samples were performed on the tribo-corrosion device (MFT-EC 4000, China) equipped with the linear reciprocating motion module, such as Fig. 1. The saturated Ag/AgCl electrode, the graphite, and the samples were served as RE, CE, and WE in turn. Prior to TC tests, standing time of ~1 h was requested to obtain a relatively stable OCP. The Al_2O_3 ball (Φ 6 mm) was served as the sliding friction pair under a normal load of 5 N. The duration of the tribo-corrosion process was 30 min under a sliding frequency of 0.1 Hz and a single sliding distance of 5 mm. All the tribo-corrosion tests for each sample were performed at least twice to obtain a true result. After TC test, the morphology and element distribution of wear track were investigated by FESEM and EDS. The three-dimensional profilometer (Rtec 3041) was applied to measure the wear volume loss. The following equation was used to evaluate the wear rate (W_R) of samples:

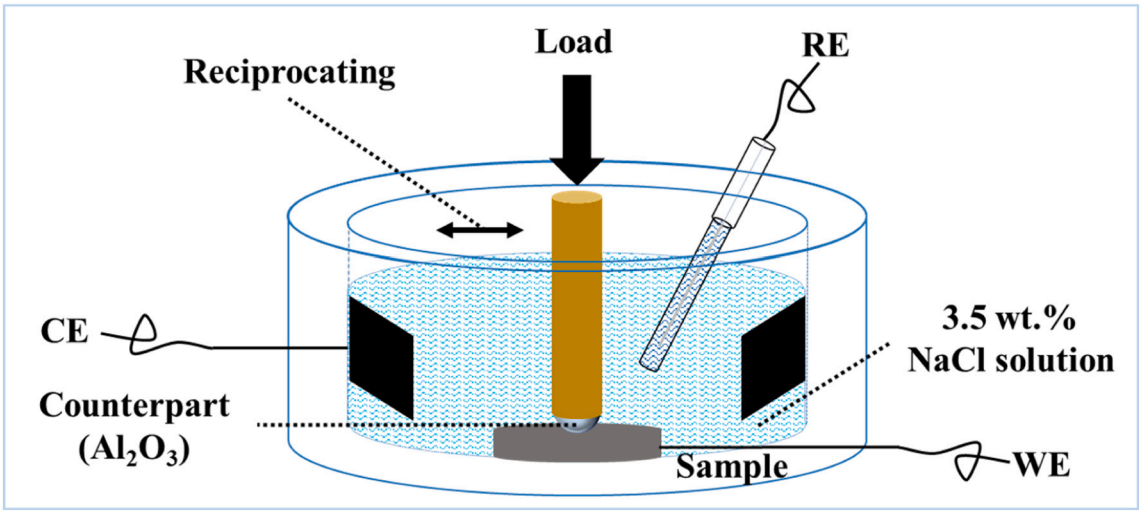

Fig. 1. Schematic diagram of the reciprocating tribo-corrosion device.

$$W_R = \frac{V_T}{N \cdot L} \tag{2}$$

where V_T, L and N are the total volume loss, sliding distance and the applied load, respectively.

3. Results and discussions

3.1. Composition and deposition rate analysis

The compositions of (CrNbTiAlV)N_x films prepared at different substrate bias are shown in Fig. 2a. Clearly seen that all samples have similar element content, indicating that the change of substrate bias has no obvious effect on the element compositions of films. The nitrogen content for all films ranges between ~40 and 43 at. % (x ≈ 0.80–0.86). The composition difference between the elements depends on the sputtering yield of each element under Argon ion bombardment [25]. Among the five metal elements, Cr element has the highest content of 22 at. %, which is attributed to its high sputtering yield. Moreover, the introduction of Cr interlayer is also one of the possible factors for its high content. The calculation formula of the mixing entropy ($\triangle S_{mix}$) in multi-principal systems is as follows [26].

$$\Delta S_{mix} = -R\sum_{i=1}^{n} c_i \mathrm{Ln} c_i \tag{3}$$

where R is the gas constant, c_i is the atomic percentage of the i_{th} element content. In this study, the nitride films own a high value of $\triangle S_{mix}$ around 13 kJ·mol^{-1} (>1.5R). Generally, the high mixing entropy can decrease the free energy and order degree of multi-principal system, which makes it easier to form random solid solutions rather than ordered phases [27].

Fig. 2b shows the deposition rate of (CrNbTiAlV)N_x films prepared under various substrate bias. Clearly, as the addition of substrate bias, the deposition rate is gradually decreased from 10.8 nm/min to 7.1 nm/min. This reduction is predominantly ascribed to the re-sputtering densification for the PVD films, which is closely bound up an increase in the energy of ions during deposition process [28]. The energy of ions bombardment (U_k) is related to the following formula [29].

$$U_k \propto \frac{D_w V_s}{P^{0.5}} \tag{4}$$

where, D_w is the power density of target, V_s is the substrate bias and P is the working pressure. Due to the P and D_w are served as a constant in this study, the U_k is directly proportional to V_s.

3.2. Phase and microstructure analysis

The XRD diagrams of (CrNbTiAlV)N_x films deposited at various substrate bias are shown in Fig. 3. Based on XRD analysis, four

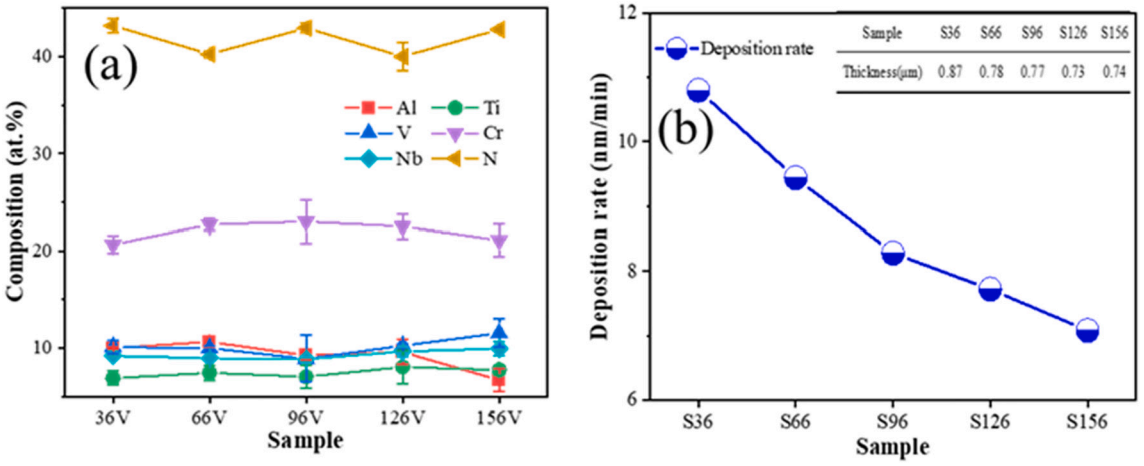

Fig. 2. Compositions (a), and deposition rates (b) of (CrNbTiAlV)N_x films prepared at different substrate bias.

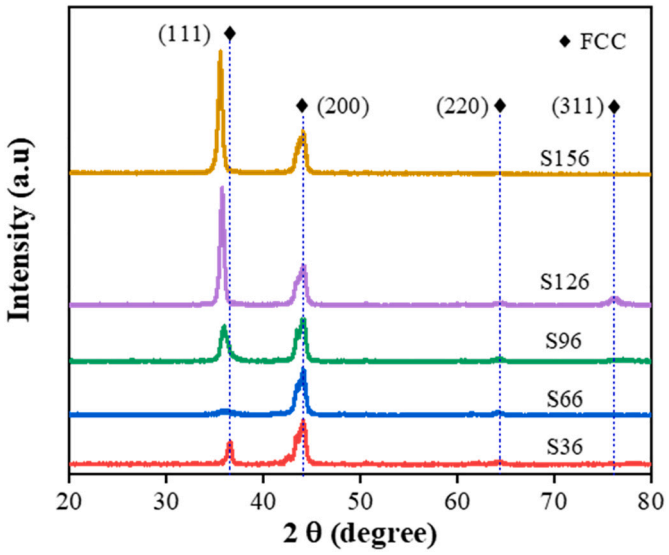

Fig. 3. XRD diagrams of (CrNbTiAlV)N_x films prepared at different substrate bias.

diffraction peaks of (111), (200), (220), (311) with simple fcc phase are found. Despite the difference in structure of metal elements, the HENFs present a single fcc solid solution phase. This phenomenon can be explained from the following two aspects. On the one hand, the selected elements are all nitride forming elements and CrN, NbN, TiN and VN have same fcc structures as listed in Table 1. On the other hand, the high mixing entropy and large atomic size difference can promote the formation of solid solution in above mentioned. From XRD diagrams, an obvious preferred orientation from (200) to (111) can be seen with the increase of substrate bias, which corresponds with the change of diffraction peak intensity. The formation of preferred orientation is related to the overall energy of film, which is the sum of surface energy and strain energy. As to fcc nitrides, (111) and (200) planes have the lowest strain energy and surface energy, respectively, and they grow in competition [30]. The surface energy is dominant under low bias, so the crystal orientation tends to grow along (200) planes. Additionally, the internal stress can induce a great strain energy in film [31]. The (111) preferred orientation is formed under high bias deposition condition, in which the strain energy plays a leading role due to the increase of stress.

According to Scherrer equation [32], the grain size calculated from the film (111) and (200) planes presents a consistent change trend, which decreases first and then increases with the increase of substrate bias, as shown in Table 3. Grain size is closely related to the half width of the diffraction peak. Compared with S36, the (111) diffraction peak of S66 is wider and its intensity is lower. It is well known that peak broadening may be due to decreasing grain size and increasing lattice strain [33]. Among these films, S66 has the smallest average grain size of 10.18 nm. The intensity of diffraction peak increases with the increase of substrate bias, indicating that the crystallinity of the film is enhanced. Previous studies have shown that higher ionic energy help adsorbed atoms migrate to a stable position on the substrate surface, thus further improving the crystallinity of the film [34]. Besides, it can be found the XRD peak shifts to the low angle direction, which may be attributed to the increase of residual stress in the films [35]. This is better illustrated by the increase in lattice parameters, as listed in Table 3.

Table 3
Relative intensity of diffraction peaks, grain size and lattice constant of (CrNbTiAlV)N_x films.

Sample	Relative intensity		Grain size (nm)		Average grain size (nm)	Lattice constant (Å)
	(111)	(200)	(111)	(200)		
S36	71	146	20.69	11.10	15.89	4.24837
S66	12	229	10.06	10.30	10.18	4.31385
S96	162	211	11.94	9.57	10.75	4.31818
S126	649	214	18.55	10.24	14.39	4.34675
S156	656	210	17.63	10.07	13.94	4.36615

Fig. 4 presents the cross-section, surface morphology and AFM images of (CrNbTiAlV)N_x films with different substrate bias. The prepared films have a typical columnar growth structure (such as Fig. 4a, b). With the increase of substrate bias, the wide column is gradually refined, thus obtaining a more compact structure (Fig. 4c, d), which is consistent with some reported nitride films [19,36]. The densification of the structure is attributed to the increased ion bombardment, which can improve the mobility of surface atoms to fill the voids and holes of the growth film and inhibit the formation of columnar structures [37]. As can be seen from the surface SEM images of Fig. 4f, g, approximately spherical particles are irregularly stacked on the surface of the film, and some micropores are detected between the particles. With increased in substrate bias, these particles appear slightly refined at first, but then increase. This change of surface morphology may be related to high-energy ion bombardment and the evolution of preferred crystal orientation, as described in the XRD analysis above. As seen in Fig. 4k–o, the evolution of AFM image further supports the above SEM morphology analysis. Furthermore, there is an initial reduction in surface RMS roughness with the increase of bias. The minimum roughness is 3.706 nm at −96 V, beyond which the roughness increases, rising to 5.384 nm at −156 V. The increased roughness may be due to ion damage to the film surface under high substrate bias [28].

3.3. Mechanical properties

As shown in Fig. 5a, all experimental samples have a compressive residual stress rising from −0.27 to −6.41 GPa with the increase of substrate bias. Many anti-Schottky defects and Frenkel pairs will be generated with the ion bombardment on the growing film during deposition [38]. The increased ion bombardment with substrate bias can trap surface atoms deeper into the film and cause more defects, which will expand the lattice and further induce high residual compressive stress [39]. Generally, these residual stresses are due to the atomic-peening effect, in which surface atoms are trapped deeper in the film by bombarding ions. The hardness and modulus of these experimental samples are positively correlated with substrate bias, as presented in Fig. 5b. The hardness and modulus increase from 17.8 to 35.3 GPa, 276.3 to 353.7 GPa with bias, respectively. It is well known that many factors can affect the mechanical properties of materials, such as elemental composition, phase structure, microstructure, preferred orientation and residual stress, etc. [28,38,40]. In the abovementioned analysis, EDS results show that the substrate bias has no significant effect on the composition of (CrNbTiAlV)N_x films. All films show single fcc phase presented from the XRD diagrams. Therefore, the elemental composition and phase structure should not be the main reason for the increase of the hardness of the film with the substrate bias. The microstructure of (CrNbTiAlV)N_x films transforms from loose columnar structure to compact structure with the increase of substrate bias. Meanwhile, the increased ion bombardment results in higher residual compressive stress in the films Also, it is worth that the film presents a preferred orientation from (200) to (111) with the increase of substrate bias, which means that more grains will grow along the direction of [111]. For the fcc nitride film, (111) with close-packed plane of atoms is also expected to improve its hardness. Based on the above analysis, the internal mechanism of increasing hardness is mainly attributed to the densification of the film, the change of residual compressive stress and the formation of (111) preferred growth.

Fig. 6 shows the scratch curves and scratch morphologies of the (CrNbTiAlV)N_x films prepared at different substrate bias. Four failure modes appear successively on the film surface during the scratch test, namely, semicircular crack, edge chipping, spallation and complete

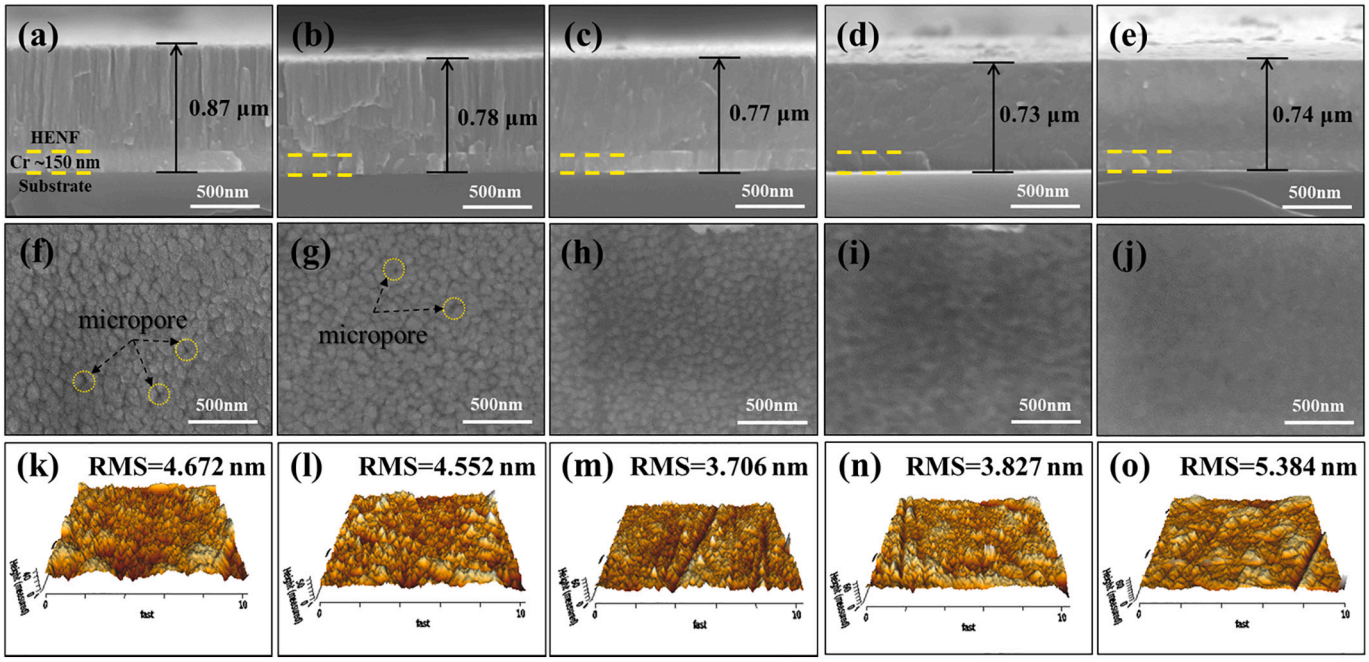

Fig. 4. SEM cross-section, surface morphologies and AFM images of (CrNbTiAlV)N_x films deposited under different substrate bias: S36 (a, f, k); S66 (b, g, l); S96 (c, h, m); S126 (d, i, n); S156 (e, j, o).

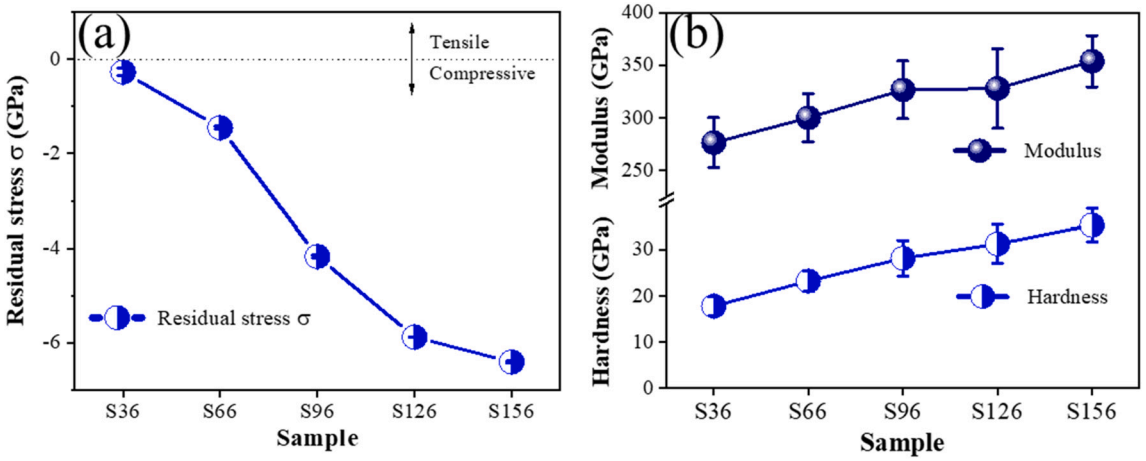

Fig. 5. Residual stress (a), hardness and elastic modulus (b) of (CrNbTiAlV)N_x films prepared with different substrate bias.

exposure of the substrate (such as in Fig. 6e). The similar phenomenon was reported in previous research [41]. L_{C1} and L_{C2} are defined as the critical load corresponding to the occurrence of semicircular crack and spallation, respectively, and marked at feature points. Interestingly, no obvious semicircular crack is detected on the scratch surface of sample S36, while the L_{C1} value of other samples was about 11 N, which may be caused by the increase of residual stress and brittleness. Moreover, the L_{C2} is usually used to evaluate the worn−through resistance of film materials. Fig. 6f presents the adhesion L_{C2} values of the films. Clearly seen that the adhesion value of films decreases with the increase of substrate bias, which may be mainly due to the increased residual stress. In other words, the increase of substrate bias leads to the increase of the residual compressive stress of the film, which improves the hardness of the film to a certain extent at the expense of the adhesion of the film. Nevertheless, all films still show high adhesion (>70 N).

3.4. Corrosion behaviors

Fig. 7 shows the Tafel curves of substrate and (CrNbTiAlV)N_x films prepared under various substrate bias. Clearly seen that all samples exhibit the active-pseudo passive characteristics and pitting behavior at E_{pit}. It is well-known that materials with more positive E_{corr} and lower i_{corr} possess better corrosion resistance [42]. The values of E_{corr} and i_{corr} obtained by Tafel extrapolation are listed in Table 4. Compared with substrate, the deposited nitride films have a positive E_{corr}, which increases from −0.557 to −0.05 V. However, there is initially an increase in i_{corr}, with a maximum of 0.385 μA/cm^2 appearing at −66 V, after that the i_{corr} decreases greatly, with a minimum of 0.013 μA/cm^2 at −126 V, beyond which the i_{corr} increases again, reaching 0.299 μA/cm^2 at −156 V. As for the films deposited at low substrate bias, the loose columnar structure provides favorable conditions for the permeation of the corrosive medium to substrate, resulting in an increase of i_{corr}. In contrast, the films prepared at −96 V and −126 V have compact nanocrystal structure, which can effectively prevent the diffusion of corrosive

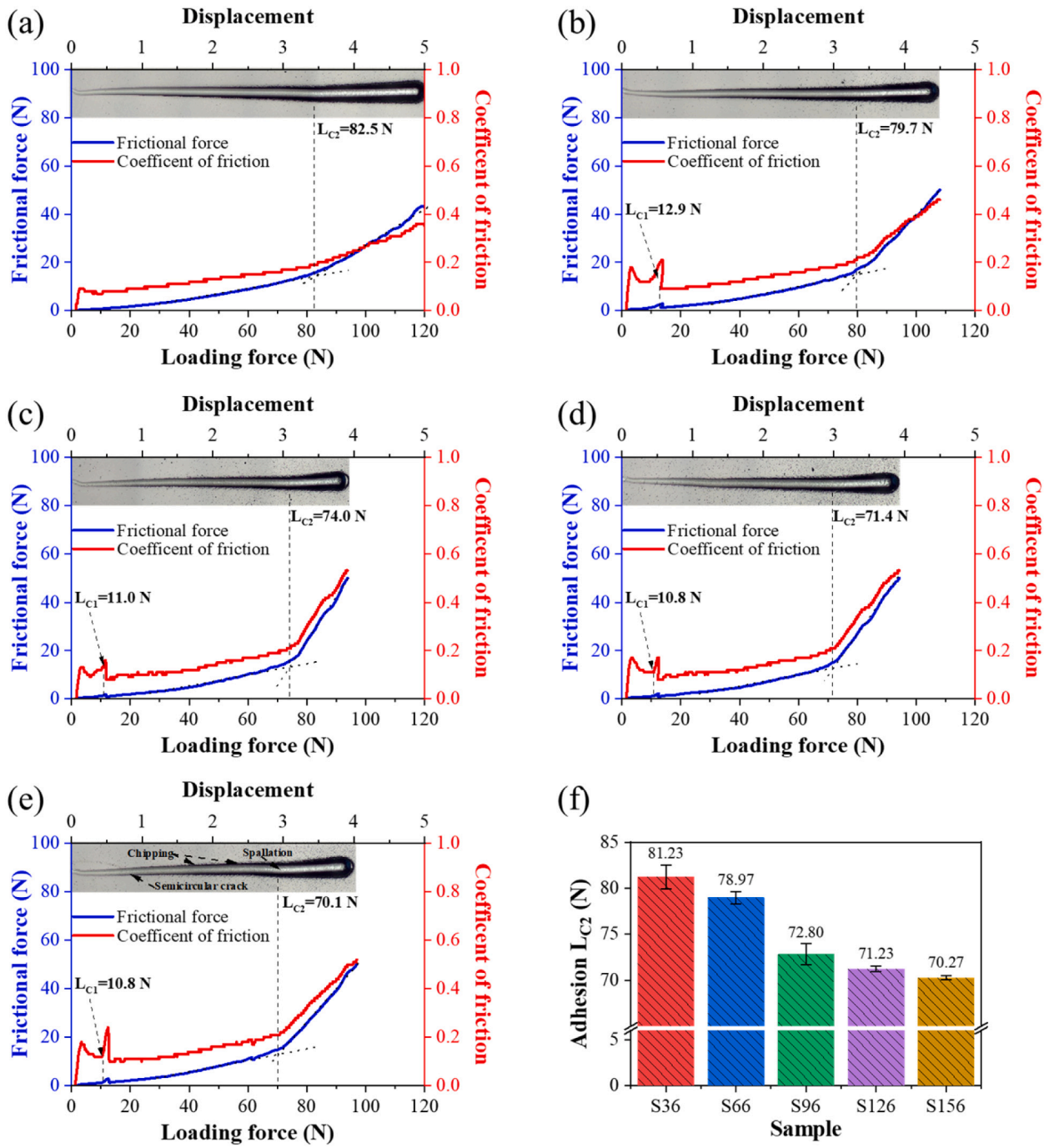

Fig. 6. The scratch curves (a: S36, b: S66, c: S96, d: S126, e: S156) and adhesion strength L_{C2} (f) of (CrNbTiAlV)N_x films deposited under different substrate bias using scratch tester with a diamond indenter (loading rate and termination load are 100 N/min and 120 N, respectively).

medium, thus generating a lower i_{corr}. The main reason affecting the corrosion resistance of S156 is pitting. Under higher bias, high-energy ion bombardment and re-sputtering effect may damage the surface of the film, which is manifested by increased surface roughness (Fig. 4o). Surface morphology significantly affects the pitting susceptibility of the materials in Cl^- containing solution [43–45]. Burstein et al. [44] found that metastable pitting was relatively difficult to form on smoother surfaces. However, once formed, it had a greater likelihood of converting to stable pitting than that formed on rough surfaces. Li et al. [45] pointed out that roughness can reduce the overall electronic work function, but the increased local fluctuations promote the formation of surface microelectrodes, thus accelerating the corrosion. Besides, higher substrate bias may cause S156 to generate more point defects during film growth, such as anti-Schottky defects and Frenkel pairs, which is manifested by the increase of residual stress [38–40]. The investigation of Zhang et al. [46,47] suggested that the formation more point defects significantly decreased the stability of passive films. According to the above analysis, the decrease of corrosion resistance of S156 may be attributed to the increased surface roughness and the formation of more point defects. The results reveal that the electrochemical properties of (CrNbTiAlV)N_x films are improved to some extent with the increase of substrate bias, but the performance will decline when the bias exceeds a certain value.

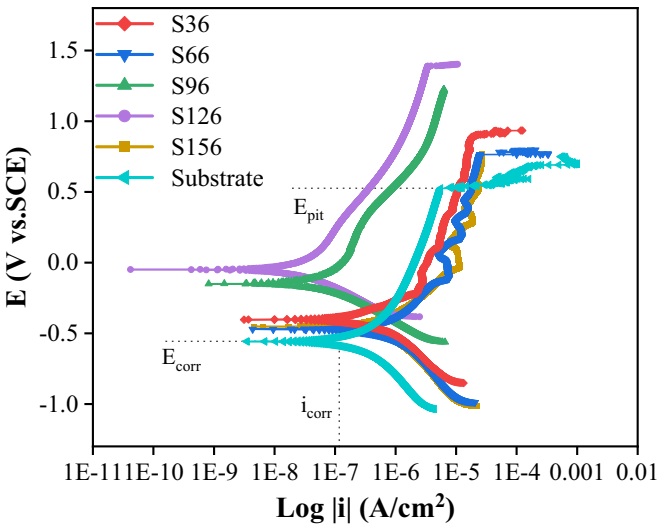

Fig. 7. The Tafel curves of substrate and $(CrNbTiAlV)N_x$ films deposited at different substrate bias in artificial seawater.

Table 4
The electrochemical parameters fitted from the polarization curve by Cview software.

Sample	E_{corr} (V_{SCE})	i_{corr} (μA/cm²)	R_{corr} (μm/PY)
S36	−0.399	0.121	1.425
S66	−0.472	0.385	4.529
S96	−0.151	0.037	0.439
S126	−0.050	0.013	0.153
S156	−0.451	0.299	3.520
Substrate	−0.557	0.110	1.299

3.5. Tribo-corrosion behaviors

Based on the results of the above electrochemical tests, S36, S96, S126 and substrate samples were selected to investigate their tribo-corrosion behaviors in artificial seawater. Fig. 8a shows the evolutions of the OCP and COF of selected samples before, during, and after tribo-corrosion test. After approximately 1 h of open circuit stabilization, all samples show relatively stable OCP, increasing in order of S36, substrate, S126 and S96, before tribo-corrosion stage (first 10 min). When loaded, the established stable state is out of balance due to the removal of the passivation film [48], which is reflected by a reduction in OCP for all samples, as shown in the enlarged image at the dotted blue line. During sliding stage (middle 30 min), all the OCP of samples decreases continuously and fluctuates (especially the substrate) under the action of friction, which can be explained by the competitive rate between the dissolution and regeneration of the passivation film [49]. Fig. 8b records the COF at the stable friction curve of the experimental samples in artificial seawater. Compared with the substrate, the nitride film (S36) prepared at low bias has a higher COF. In contrast, the films (S96 and S126) at medium bias exhibit lower COF ranging from 0.2 to 0.25, which mean their favorable tribological properties under OCP condition. Once unloaded (final 10 min), the passivation film in generation rate is greater than the dissolution rate, so the values of OCP increase and gradually stabilize, as shown in the enlarged image at the dotted black line. Among these experimental samples, the S96 exhibits the highest OCP value before, during and after the sliding process, indicating its excellent tribo-corrosion behaviors.

As shown in Fig. 9a–d, the wear depth of S36, S96, S126 and substrate is about 200 nm, 130 nm, 50 nm and 450 nm, respectively. The trend of wear width is consistent with the wear depth, decreasing from 260 nm of substrate to 67 nm of S126. The wear rate of these experimental samples is presented in Fig. 8b. Clearly seen that the substrate has the highest wear rate of 3.16×10^{-5} $mm^3 \cdot N^{-1} \cdot m^{-1}$. In contrast, the wear rate of nitride films is not only low, but also significantly decreases with the increasing bias, and the minimum value is 4.4×10^{-7} $mm^3 \cdot N^{-1} \cdot m^{-1}$ occurring at −126 V. Based on the above analysis, S126 sample has compact structure, residual compressive stress, good adhesion and higher hardness, so it has a lower wear rate.

To further analyze its tribo-corrosion mechanism, the surface morphologies of wear track are investigated by SEM. As seen in Fig. 9d1, the surface morphology of the substrate shows a plow shape, which infers that the wear mechanism should be abrasive wear. The rough surface caused by the ploughing effect keeps the COF at a high value. Furthermore, many microcracks caused by plastic deformation are observed on the wear surface. These microcracks are conducive to the diffusion of chloride ions, which resulted in the continuous decrease of OCP. The wear surface of the nitride film rarely shows microcracks, but brittle spallation. Among these nitride films, S36 exhibits the worst tribo-corrosion performance. As shown in Fig. 9a1, large groove appears on the surface of the wear track, which not only causes a large COF, but also increases the fluctuation of COF during the friction process. Besides, the formation of grooves will further aggravate the corrosion of materials. With a columnar structure at low bias, a large amount of pitting is generated, resulting in a lower OCP. For the films prepared under medium bias, as can be seen from Fig. 9b1, the wear surface of S96 is dense

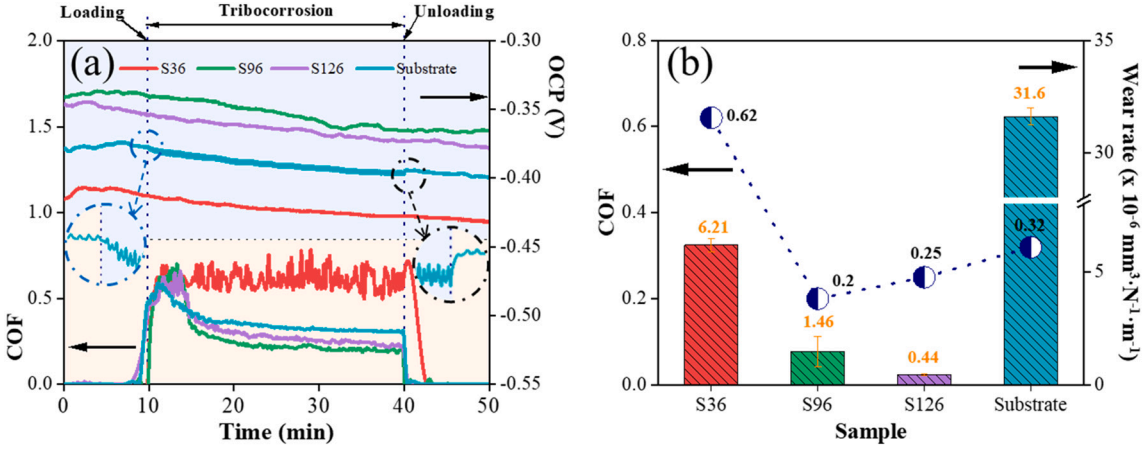

Fig. 8. Evolution of the open circuit potential (OCP vs. Ag/AgCl) and coefficient of friction (COF) in before, during, and after tribo-corrosion (a), the wear rate and friction coefficient (b) of substrate and $(CrNbTiAlV)N_x$ films using tribo-corrosion device with a 6 mm diameter sliding friction pair Al_2O_3 ball (the normal load, sliding time, sliding frequency and unidirectional sliding length are 5 N, 30 min, 0.1 Hz and 5 mm, respectively).

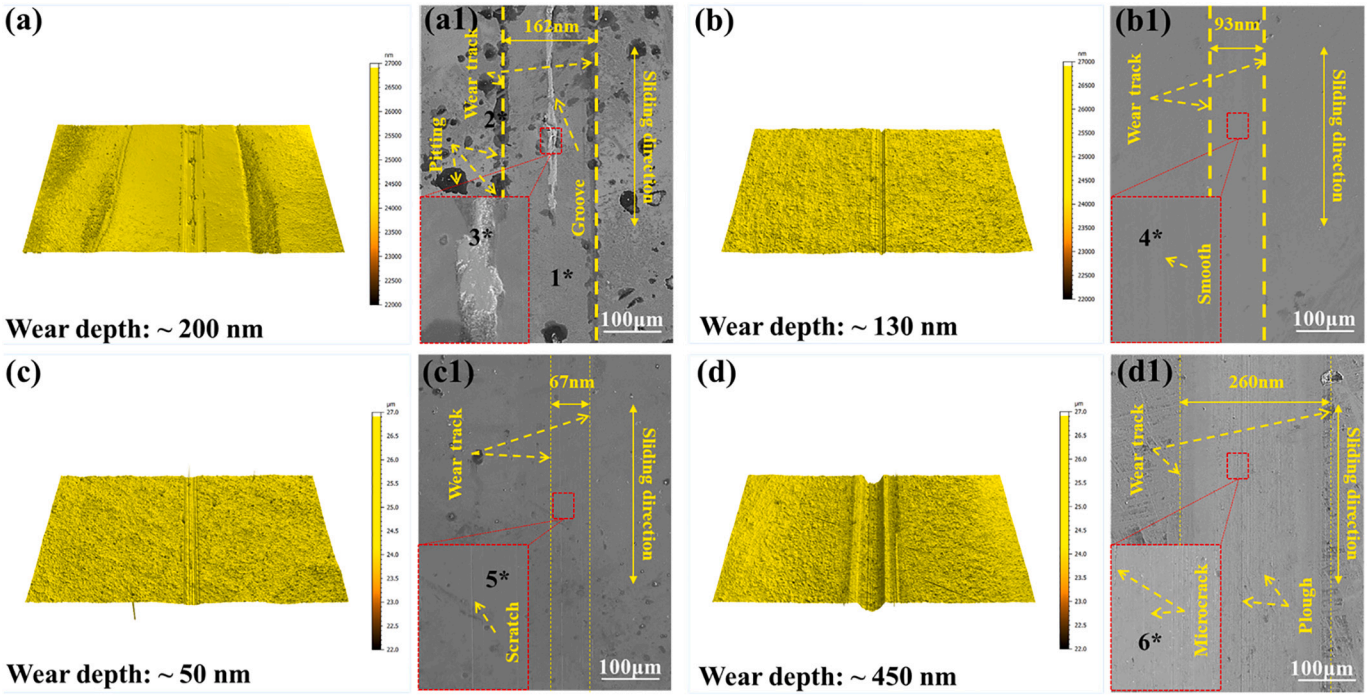

Fig. 9. Three-dimensional profiles and SEM images for wear track of S36 (a, a1), S96 (b, b1), S126 (c, c1) and substrate (d, d1) after tribo-corrosion tests.

and smooth, promoting its high OCP and low COF. But S126 has some brittle scratching on its wear surface (Fig. 9c1), which may be the reason for its coefficient of friction slightly higher than that of S96. Table 5 lists the distribution of elements at selected points on the wear by EDS. The oxygen content on the substrate surface is significantly higher than that of the nitride film. Among them, the films at medium bias have similar EDS results and show almost no oxygen element. In brief, both S96 and S126 possess an excellent tribo-corrosion property.

Based on the above analysis, the corrosion and tribological mechanism of the (CrNbTiAlV)N_x nitride films under static and tribo-corrosion condition is illustrated in Fig. 10. In static corrosion condition, the columnar structure of the films prepared under low bias decreases the corrosion resistance. The tissue becomes compact and its corrosion resistance is improved by adjusting the bias. Under tribo-corrosion condition, the film at low bias has low hardness and wear seriously. Hard nitride debris generated by friction increases its COF. Furthermore, the spallation on the wear surface can further accelerate the diffusion of the corrosive medium, thus exhibiting a lower OCP. On the contrary, the hardness of film under the medium bias is higher and the wear rate is lower. The high OCP and low COF were exhibited due to the dense and smooth wear morphology.

4. Conclusion

Based on the analysis of the microstructure, mechanical, electrochemical and tribo-corrosion properties of the multi-element (CrNbTiAlV)N_x high-entropy nitride films prepared under different substrate bias, the main conclusions are drawn as follows:

(1) The multi-element (CrNbTiAlV)N_x nitride films present a single fcc solid solution structure. The microstructure of the films changes from columnar to compact, accompanied by a preferred orientation from (200) to (111) with the increase of substrate bias.

(2) The residual stress of all films is in a state of compression. With the increase in substrate bias, the hardness of the prepared films increases from 17.8 to 35.3 GPa, which is mainly due to the densification of the film, the change of residual compressive stress and the formation of (111) preferred growth. The adhesion of all samples is greater than 70 N.

(3) Static electrochemical experiments show that the films prepared by medium bias have better corrosion resistance than those prepared by low bias, because the compact nanocrystal structure of the former can hinder and delay the arrival of corrosive media to the substrate. Among them, S126 exhibits the best electrochemical performance.

(4) The tribo-corrosion properties of the experimental films are improved under substrate bias. S96 has the highest OCP and the lowest COF of ~0.2, which can be attributed to the compact and smooth surface of wear track. Higher hardness is beneficial to improve wear resistance, and S126 has the lowest wear rate of $\sim 4.4 \times 10^{-7}$ $mm^3 \cdot N^{-1} \cdot m^{-1}$.

Table 5
EDS results of selected points on the wear track after the tribo-corrosion tests (at. %).

Sample	Point	N	O	Al	Ti	V	Cr	Nb	Fe
	1	39.4	5.8	9.5	6.7	9.4	21.1	8.2	–
S36	2	–	25.8	14.5	9.3	11.8	26.4	12.3	–
	3	34.3	1.2	10.9	7.6	10.8	25.4	9.7	–
S96	4	37.3	–	8.9	6.7	10.3	26.3	10.6	–
S126	5	36.6	–	8.4	7.5	10.5	26.9	10.2	–
Substrate	6	–	57.5	–	–	–	–	–	42.5

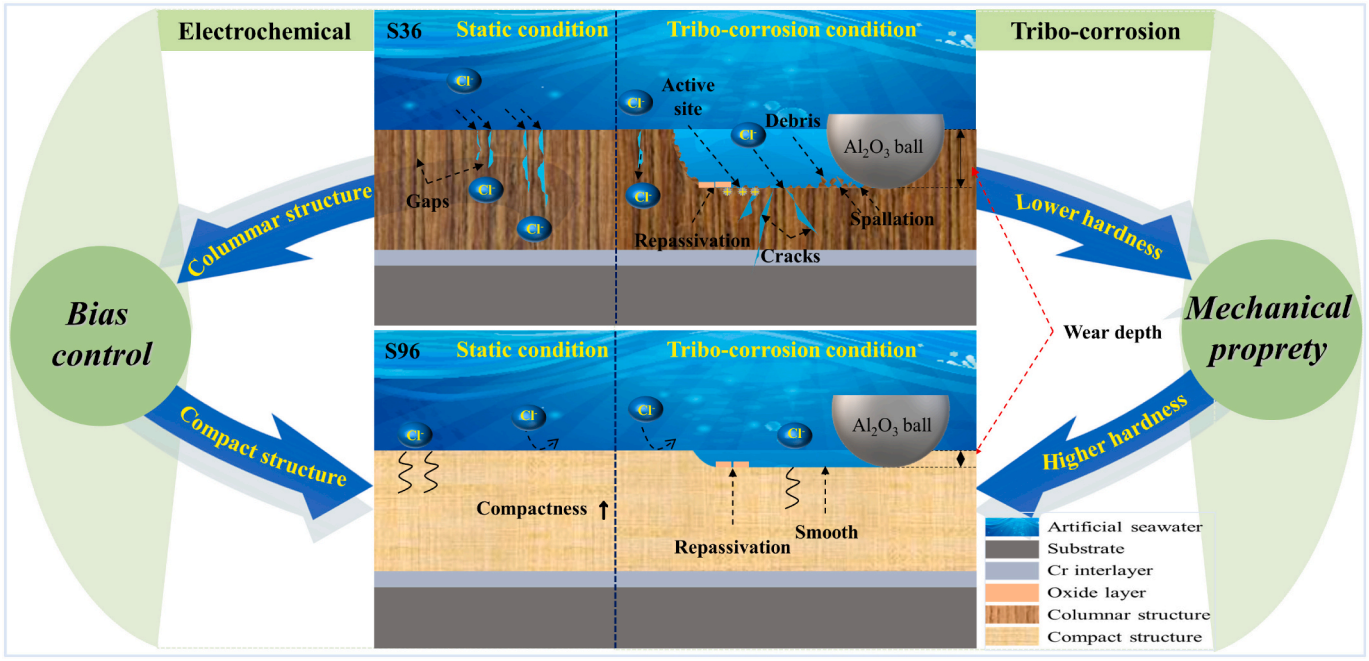

Fig. 10. Schematic of the corrosion and tribological mechanism of the (CrNbTiAlV)N_x films under different work condition.

CRediT authorship contribution statement

Cunxiu Zhang: Conceptualization, Methodology, Investigation, Validation, Formal analysis, Writing – original draft, Visualization. **Xiaolong Lu:** Investigation. **Haibin Zhou:** Investigation. **Yanfang Wang:** Resources, Writing – review & editing, Funding acquisition. **Xudong Sui:** Resources, Writing – review & editing, Funding acquisition. **ZhiQiang Shi:** Resources, Writing – review & editing, Funding acquisition. **Junying Hao:** Resources, Writing – review & editing, Supervision, Funding acquisition.

Declaration of competing interest

All the authors declare no competing financial interest for this paper.

Acknowledgement

The authors gratefully acknowledge the financial support of National Natural Science Foundation of China (51835012, 51975554), the National Key Research and Development Program of China (No. 2018YFB0703803), the program of "Science & Technology International Cooperation Demonstrative Base of Metal Surface Engineering along the Silk Road (2017D01003)," and CAS "Light of West China".

References

[1] L. Li, L.L. Liu, X.W. Li, P. Guo, P.L. Ke, A.Y. Wang, Enhanced tribocorrosion performance of Cr/GLC multilayered films for marine protective application, ACS Appl. Mater. Interfaces 10 (2018) 13187–13198, https://doi.org/10.1021/acsami.8b00628.

[2] S.K. Pradhan, P. Bhuyan, L.R. Bairi, S. Mandal, Comprehending the role of individual microstructural features on electrochemical response and passive film behaviour in type 304 austenitic stainless steel, Corros. Sci. 180 (2021) 109187–109199, https://doi.org/10.1016/j.corsci.2020.109187.

[3] C.O.A. Olsson, D. Landolt, Passive films on stainless steels-chemistry, structure and growth, Electrochim. Acta 48 (2003) 1093–1104, https://doi.org/10.1016/S0013-4686(02)00841-1.

[4] K. Rohith, S. Shreyas, K.B. Vishnu Appaiah, R.V. Sheshank, B.B. Ganesha, B. Vinod, Recent material advancement for marine application, Mater. Today Proc. 18 (2019) 4854–4859, https://doi.org/10.1016/j.matpr.2019.07.476.

[5] C.B. von der Ohe, R. Johnsen, N. Espallargas, Multi- degradation behavior of austenitic and super duplex stainless steel – the effect of 4-point static and cyclic bending applied to a simulated seawater tribocorrosion system, Wear 288 (2012) 39–53, https://doi.org/10.1016/j.wear.2012.02.016.

[6] Y.Q. Fu, F. Zhou, Q.Z. Wang, M.D. Zhang, Z.F. Zhou, Electrochemical and tribocorrosion performances of CrMoSiCN coating on ti-6Al-4V titanium alloy in artificial seawater, Corros. Sci. 165 (2020), 108385, https://doi.org/10.1016/j.corsci.2019.108385.

[7] J.W. Yeh, S.K. Chen, S.J. Lin, J.Y. Gan, T.S. Chin, T.T. Shun, C.H. Tsau, S.Y. Chang, Nanostructured high-entropy alloys with multiple principal elements: novel alloy design concepts and outcomes, Adv. Eng. Mater. 6 (2004) 299–303, https://doi.org/10.1002/adem.200300567.

[8] Z.C. Chang, S.C. Liang, S. Han, Y.K. Chen, F.S. Shieu, Characteristics of TiVCrAlZr multi-element nitride films prepared by reactive sputtering, Nucl. Instrum. Methods Phys. Res. 268 (2010) 2504–2509, https://doi.org/10.1016/j.nimb.2010.05.039.

[9] S.C. Liang, D.C. Tsai, Z.C. Chang, H.S. Sung, Y.C. Lin, Y.J. Yeh, M.J. Deng, F. S. Shieu, Structural and mechanical properties of multi-element (TiVCrZrHf)N coatings by reactive magnetron sputtering, Appl. Surf. Sci. 258 (2011) 399–403, https://doi.org/10.1016/j.apsusc.2011.09.006.

[10] X.H. Yan, J.S. Li, W.R. Zhang, Y. Zhang, A brief review of high-entropy films, Mater. Chem. Phys. 210 (2018) 12–19, https://doi.org/10.1016/j.matchemphys.2017.07.078.

[11] E. Lewin, Multi-component and high-entropy nitride coatings-a promising field in need of a novel approach, J. Appl. Phys. 127 (2020) 160901–160913, https://doi.org/10.1063/1.5144154.

[12] R. Shu, E.M. Paschalidou, S.G. Rao, J. Lu, G. Greczynski, E. Lewin, L. Nyholmb, A. L. Febvrier, P. Eklund, Microstructure and mechanical, electrical, and electrochemical properties of sputter-deposited multicomponent (TiNbZrTa)Nx coatings, Surf. Coat. Technol. 389 (2020) 125651–125658, https://doi.org/10.1016/j.surfcoat.2020.125651.

[13] K. von Fieandt, L. Riekehr, B. Osinger, S. Fritze, E. Lewin, Influence of N content on structure and mechanical properties of multi- component Al-cr-nb-Y-zr based thin films by reactive magnetron sputtering, Surf. Coat. Technol. 389 (2020), 125614, https://doi.org/10.1016/j.surfcoat.2020.125614.

[14] X.G. Feng, K.F. Zhang, Y.G. Zheng, H. Zhou, Z.H. Wan, Chemical state, structure and mechanical properties of multi-element (CrTaNbMoV)Nx films by reactive magnetron sputtering, Mater. Chem. Phys. 239 (2020), 121991, https://doi.org/10.1016/j.matchemphys.2019.121991.

[15] R. Chen, Z.B. Cai, J.B. Pu, Z.X. Lu, S.Y. Chen, S.J. Zheng, C. Zeng, Effects of nitriding on the microstructure and properties of VAlTiCrMo high-entropy alloy coatings by sputtering technique, J. Alloys Compd. 827 (2020) 153836–153843, https://doi.org/10.1016/j.jallcom.2020.153836.

[16] L.Q. Chen, W. Li, P. Liu, K. Zhang, F.C. Ma, X.H. Chen, H.L. Zhou, X.K liu, microstructure and mechanical properties of (AlCrTiZrV)Nx high-entropy alloy nitride films by reactive magnetron sputtering, Vacuum 181 (2020) 109706–109712, https://doi.org/10.1016/j.vacuum.2020.109706.

[17] H. Chen, Y.W. Ye, C.T. Wang, X.L. Ma, H.X. Wang, W. Liu, Understanding the corrosion and tribological behaviors of CrSiN coatings with various Si contents in HCl solution, Tribol. Int. 131 (2019) 530–540, https://doi.org/10.1016/j.triboint.2018.11.018.

[18] Q.Z. Wang, F. Zhou, Z.F. Zhou, L.K.Y. Li, J.W. Yan, Influence of carbon concentration on the electrochemical behavior of CrCN coatings in simulated body

fluid, Surf. Coat. Technol. 265 (2015) 16–23, https://doi.org/10.1016/j.bbr.2014.11.040.
[19] W.J. Shen, M.H. Tsai, Y.S. Chang, J.W. Yeh, Effects of substrate bias on the structure and mechanical properties of (Al1.5CrNb0.5Si0.5Ti)Nx coatings, Thin Solid Films 520 (2012) 6183–6188, https://doi.org/10.1016/j.tsf.2012.06.002.
[20] H.T. Hsueh, W.J. Shen, M.H. Tsai, J.W. Yeh, Effect of nitrogen content and substrate bias on mechanical and corrosion properties of high-entropy films (AlCrSiTiZr)100-xNx, Surf. Coat. Technol. 206 (2012) 4106–4112, https://doi.org/10.1016/j.surfcoat.2012.03.096.
[21] X.L. Lu, C.X. Zhang, C. Wang, X.J. Cao, R. Ma, X.D. Sui, J.Y. Hao, W.M. Liu, Investigation of (CrAlTiNbV)Nx high-entropy nitride coatings via tailoring nitrogen flow rate for anti-wear applications in aviation lubricant, Appl. Surf. Sci. 557 (2021), 149813, https://doi.org/10.1016/j.apsusc.2021.149813.
[22] S. Guo, C.T. Liu, Phase stability in high entropy alloys: formation of solid-solution phase or amorphous phase, Prog. Nat. Sci. Mater. Int. 21 (2011) 433–446, https://doi.org/10.1016/S1002-0071(12)60080-X.
[23] S.Y. Chang, S.Y. Lin, Y.C. Huang, Mechanical properties, deformation behaviors and interface adhesion of (AlCrTaTiZr)Nx multi-component coatings, Surf. Coat. Technol. 204 (2010) 3307–3314, https://doi.org/10.1016/j.surfcoat.2010.03.041.
[24] G.G. Stoney, The tension of metallic films deposited by electrolysis, Proc. R. Soc. AMath. Phys. 82 (1909) 172–175, https://doi.org/10.1098/rspa.1909.0021.
[25] L. Aissani, A. Alhussein, C. Nouveau, L. Radjehi, I. Lakdhar, E. Zgheib, Evolution of microstructure, mechanical and tribological properties of vanadium carbonitride coatings sputtered at different nitrogen partial pressures, Surf. Coat. Technol. 374 (2019) 531–540, https://doi.org/10.1016/j.surfcoat.2019.06.034.
[26] Y. Zhang, Y.J. Zhou, J.P. Lin, G.L. Chen, P.K. Liaw, Solid-solution phase formation rules for multi-component alloys, Adv. Eng. Mater. 10 (2008) 534–538, https://doi.org/10.1002/adem.200700240.
[27] D.C. Tsai, Z.C. Chang, B.H. Kuo, M.H. Shiao, S.Y. Chang, F.S. Shieu, Structural morphology and characterization of (AlCrMoTaTi)N coating deposited via magnetron sputtering, Appl. Surf. Sci. 282 (2013) 789–797, https://doi.org/10.1016/j.apsusc.2013.06.057.
[28] C.H. Lai, S.J. Lin, J.W. Yeh, A. Davison, Effect of substrate bias on the structure and properties of multi-element (AlCrTaTiZr)N coatings, J. Phys. D. Appl. Phys. 39 (2006) 4628–4633.
[29] D.M. Mattox, Particle bombardment effects on thin-film deposition: a review, J. Vac. Sci. Technol. A 7 (1989) 1105–1114, https://doi.org/10.1116/1.576238.
[30] U.C. Oh, J.H. Je, Effects of strain energy on the preferred orientation of TiN thin films, J. Appl. Phys. 74 (1993) 1692–1696, https://doi.org/10.1063/1.355297.
[31] D.S. Rickerby, A.M. Jones, B.A. Bellamy, High-temperature x-ray diffraction studies on physical vapour deposited TiN, Surf. Coat. Technol. 39 (1989) 397–408, https://doi.org/10.1016/0257-8972(89)90072-8.
[32] B. Ingham, M.F. Toney, 1-X-ray diffraction for characterizing metallic films, in: Metallic Films for Electronic, Optical and Magnetic Applications, Woodhead Publishing, 2014, pp. 3–38, https://doi.org/10.1533/9780857096296.1.3.
[33] X.G. Feng, K.F. Zhang, Y.G. Zheng, H. Zhou, Z.H. Wan, Chemical state, structure and mechanical properties of multi-element (CrTaNbMoV)Nx films by reactive magnetron sputtering, Mater. Chem. Phys. 239 (2020), 121991, https://doi.org/10.1016/j.matchemphys.2019.121991.
[34] D.M. Mattox, Particle bombardment effects on thin-film deposition: a review, J. Vac. Sci. Technol. A 7 (1989) 1105–1114, https://doi.org/10.1116/1.576238.
[35] C.H. Lai, S.J. Lin, J.W. Yeh, S.Y. Chang, Preparation and characterization of AlCrTaTiZr multi-element nitride coatings, Surf. Coat. Technol. 201 (2006) 3275–3280, https://doi.org/10.1016/j.surfcoat.2006.06.048.
[36] J.J. Wang, S.Y. Chang, F.Y. Ouyang, Effect of substrate bias on the microstructure and properties of (AlCrSiNbZr)Nx high entropy nitride thin film, Surf. Coat. Technol. 393 (2020) 125796–125806, https://doi.org/10.1016/j.surfcoat.2020.125796.
[37] K.H. Müller, Ion-beam-induced epitaxial vapor-phase growth: a molecular-dynamics study, Phys. Rev. B Condens. Matter 35 (1987) 7906–7913, https://doi.org/10.1103/PhysRevB.35.7906.
[38] W.L. Lo, S.Y. Hsu, Y.C. Lin, S.Y. Tsai, Y.T. Lai, J.G. Duh, Improvement of high entropy alloy nitride coatings (AlCrNbSiTiMo)N on mechanical and high temperature tribological properties by tuning substrate bias, Surf. Coat. Technol. 401 (2020), 126247, https://doi.org/10.1016/j.surfcoat.2020.126247.
[39] H. Oettel, R. Wiedemann, Residual stresses in PVD hard coatings, Surf. Coat. Technol. 76–77 (1995) 265–273, https://doi.org/10.1016/0257-8972(95)02581-2.
[40] X. Yu, J.J. Wang, L.Q. Wang, W.J. Huang, Fabrication and characterization of CrNbSiTiZr high-entropy alloy films by radio-frequency magnetron sputtering via tuning substrate bias, Surf. Coat. Technol. 412 (2020), 127074, https://doi.org/10.1016/j.surfcoat.2021.127074.
[41] S. Chen, K.K. Tseng, Y. Tong, W. Li, C.W. Tsai, J.W. Yeh, P.K. Liaw, Grain growth and hall-petch relationship in a refractory HfNbTaZrTi high-entropy alloy, J. Alloys Compd. 795 (2019) 19–26, https://doi.org/10.1016/j.jallcom.2019.04.291.
[42] S.J. Zheng, Z.B. Cai, J.B. Pu, C. Zeng, S.Y. Chen, R. Chen, L.P. Wang, A feasible method for the fabrication of VAlTiCrSi amorphous high entropy alloy film with outstanding anti-corrosion property, Appl. Surf. Sci. 483 (2019) 870–874, https://doi.org/10.1016/j.apsusc.2019.03.338.
[43] S. Lee, W. Lee, Y. Kim, H. Jang, Surface roughness and the corrosion resistance of 21Cr ferritic stainless steel, Corros. Sci. 63 (2012) 404–409, https://doi.org/10.1016/j.corsci.2012.06.031.
[44] G. Burstein, S. Vines, Repetitive nucleation of corrosion pits on stainless steel and the effects of surface roughness, J. Electrochem. Soc. 148 (2001) B504–B516, https://doi.org/10.1149/1.1416503.
[45] W. Li, D. Li, Influence of surface morphology on corrosion and electronic behavior, Acta Mater. 54 (2006) 445–452, https://doi.org/10.1016/j.actamat.2005.09.017.
[46] C. Zhang, K. Chan, Y. Wu, L. Liu, Pitting initiation in Fe-based amorphous coatings, Acta Mater. 60 (2012) 4152–4159.
[47] C. Zhang, Z. Zhang, Q. Chen, L. Liu, Effect of hydrostatic pressure on the corrosion behavior of HVOF-sprayed Fe-based amorphous coating, J. Alloy. Compd. 758 (2018) 108–115, https://doi.org/10.1016/j.jallcom.2018.05.100.
[48] A. Hatem, J.L. Lin, R.H. Wei, R.D. Torres, C. Laurindo, G.B.D. Souza, P. Soares, Tribocorrosion behavior of low friction TiSiCN nanocomposite coatings deposited on titanium alloy for biomedical applications, Surf. Coat. Technol. 347 (2018) 1–12, https://doi.org/10.1016/j.surfcoat.2018.04.049.
[49] Y.Q. Fu, F. Zhou, Q.Z. Wang, M.D. Zhang, Z.F. Zhou, Electrochemical and tribo-corrosion performances of CrMoSiCN coating on Ti-6Al-4V titanium alloy in artificial seawater, Corros. Sci. 165 (2020) 108385–108397, https://doi.org/10.1016/j.corsci.2019.108385.